Strong-field control by reverse engineering

Attila Tóth
ELI-ALPS, ELI-HU Non-Profit Ltd., Wolfgang Sandner utca 3., H-6728 Szeged, Hungary

András Csehi*
Department of Theoretical Physics, Faculty of Science and Technology, University of Debrecen, PO Box 400, 4002 Debrecen, Hungary

(Received 15 September 2021; accepted 18 November 2021; published 2 December 2021)

Based on the idea of reverse engineering, we design an optimal laser pulse to control strong-field multiphoton atomic transitions. Starting from the time-dependent Schrödinger equation of the full system, we adiabatically eliminate the nonessential states and apply the rotating-wave approximation to arrive at an effective two-state representation that involves dynamic Stark shifts and multiphoton coupling. Solving this equation inversely for the field, we obtain an analytical laser pulse shape that is expected to induce the full system's evolution according to user-defined quantum pathways. In our procedure, the amplitude and phase of the laser pulse are engineered such that the dynamically shifted electronic states are resonantly coupled during the action of the pulse at each moment of time. As a result, the driven system evolves from an arbitrary initial population distribution to any desired final quantum state superposition at a predefined rate. The proposed scheme is demonstrated using the example of the $3s \rightarrow 4s$ two-photon transition of atomic sodium. By solving the time-dependent Schrödinger equation of the single-active electron with two different methods, either propagating time-dependent coefficients of many field-free states or directly propagating the three-dimensional electronic wave packet on a grid, we demonstrate the robustness as well as the limitations of the presented reverse engineering scheme.

DOI: 10.1103/PhysRevA.104.063102

I. INTRODUCTION

Selectively steering the time evolution of atomic and molecular systems with pulsed laser fields has gained much interest over the past four decades [1–6]. Different quantum control strategies have been proposed to guide the system under consideration from its initial state to a desired final state with high efficiency. The rapid adiabatic passage and stimulated Raman adiabatic passage techniques [3] were found to be very robust for efficient population transfer when the transitions are induced by a single photon. To increase the speed of transition, shortcut to adiabaticity (STA) techniques [7–13] have been introduced. Other methods, like optimal control [14–16] and reverse engineering [17–31], have been also widely applied with great success.

In the procedure of reverse engineering, one usually introduces a control function in advance to define the desired quantum pathway of the system under control. Knowing this target function, one then solves the Schrödinger equation or some density equations inversely to obtain the form of interaction that leads to the prescribed time evolution. A great advantage of reverse engineering is that one can design optimal laser pulses in an analytical form, although only for few-level systems. The rotating-wave approximation (RWA) is usually applied during the derivations, and hence the breakdown of the RWA is a serious restriction in such a case [25,28,29]. Control methods have been proposed which do not make use of the RWA and hence allow for fast manipulation of the system dynamics [21,30].

Analytically solvable driven two-level systems are invaluable in many fields of physics as they are extremely rare [32]. Two-level systems are crucial to understanding the essential laser quantum control strategies of realistic multilevel systems [33–38]. They play a fundamental role in reverse engineering control (among others), where analytical pulse design is in focus.

In realistic systems, the two-level description may become inaccurate when the neighboring states lie energetically close and get populated during the atom-field interaction. This might become more severe in the strong-field regime where multiphoton transitions occur and the energy levels are subject to dynamic Stark shifts and thus the underlying physics is significantly modified [39,40]. Several experimental and theoretical works have shown that despite the movement of the atomic levels, efficient population transfer is possible between two electronic states upon absorption of multiple photons from the same pulse [41–58]. Most of these works deal with two-photon transitions in alkali metals and a proper modulation of the phase or shape of the laser pulse is applied to compensate for the relative dynamic Stark shift (DSS) of interest and transfer population efficiently.

Strong-field multiphoton transitions between two bound states of an atom are often accompanied by ionization upon absorption of further photon(s) from the same pulse. Such resonance-enhanced multiphoton ionization (REMPI) processes are very sensitive to the dynamic Stark shifts of the involved resonant states and usually manifest in a

*csehi.andras@science.unideb.hu

structural change of the energy spectrum of emitted electrons [59,60]. Selective excitation and subsequent ionization to distinct channels are often a central problem in the control of REMPI processes. On the example of atomic targets, selective suppression and enhancement of the ionization yield have been demonstrated using chirped laser pulses [61,62] and also unshaped ones [63–66]. Applying chirped strong-field ultrafast laser pulses, a competition between REMPI and internal conversion has been demonstrated in a polyatomic molecule [67]. In general, REMPI leads to the splitting and structuring of the spectral peaks of emitted photoelectrons [68–71]. This kind of spectral behavior is further modulated by the dynamic Stark shifts of the involved states, allowing for the tracing of strong-field transitions via the spectrum of ionized electrons [72].

In the present work we aim to control strong-field transitions in an atomic system using appropriately shaped analytical laser pulses that are obtained from a reverse engineering idea [25]. For our analysis, we will consider atomic sodium, which has been intensively studied in recent years both theoretically and experimentally [45–48,52,61,64–66,73–75]. Starting from the Schrödinger equation of the full system, we develop a two-state effective model for the $3s \rightarrow 4s$ two-photon transition upon adiabatically eliminating (AE) the nonessential states plus applying the two-photon RWA (AER). The obtained model, which involves dynamic Stark shifts and multiphoton coupling, is then used as a starting point for the inverse engineering procedure, as a result of which a single frequency-modulated laser pulse is derived. Applying this laser pulse, the system is driven from an arbitrary initial superposition of the $3s$ and $4s$ states to any desired final target population distribution. In our procedure, the rate of transition is also controlled in contrast to many other works, where only the final state is of interest, but not the quantum path that is completed by the system. To test the validity of the model and of the engineered laser pulse, we solve the time-dependent Schrödinger equation (TDSE) of the single active electron with two different methods: (i) propagating time-dependent expansion coefficients of numerous field-free states (the TDEC method) and (ii) directly propagating the electron wave packet on a grid (the TDWP method). In our analysis, we pay particular attention to the investigation of multistate effects by revealing the conditions for the selective excitation of the $4s$ state and subsequent ionization via the $7p$ near-resonant state.

II. THEORY

Let us start by introducing the theoretical framework of the strong-field two-photon transition studied in this work. We consider atomic sodium as a concrete example initially in the superposition of the $3s$ ground state ($|g\rangle$) and the $4s$ excited state ($|e\rangle$). Applying a coherent intense laser pulse (which is to be designed by reverse engineering), the system is excited by two photons to the desired final superposition of the $3s$ and $4s$ states along some user-defined control function (see Fig. 1). The field-free atom is represented by the Hamiltonian H_0 and its corresponding eigenstates $|j\rangle$ and eigenenergies ω_j (atomic units are used), where the j index runs over all the states of the atom. The interaction of the atom with the laser pulse is

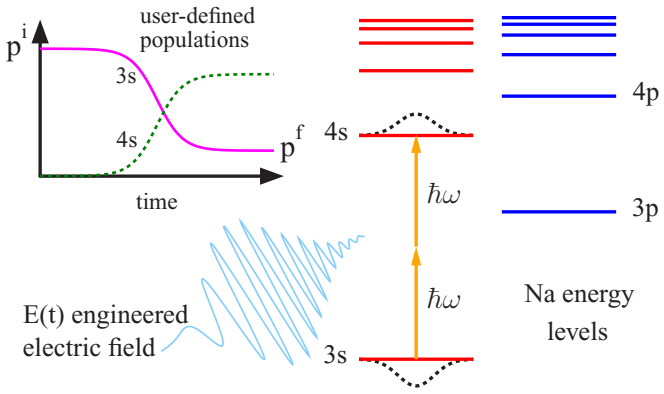

FIG. 1. Schematic representation of the strong-field two-photon control scenario discussed in this work. The shaped laser pulse $E(t)$, which is obtained by reverse engineering, interacts with the atomic target and induces its time evolution according to a prescribed quantum path. The amplitude and phase of $E(t)$ are engineered such that the relative dynamic Stark shift of interest, $3s$-$4s$ in the case of Na, is fully compensated and an efficient population transfer is achieved, which leads to the desired final quantum state superposition of the system. The bell-shaped dashed lines symbolize the dynamic Stark shifts of the strongly coupled states.

treated in the dipole approximation, that is, $V(t) = -\vec{\mu} \cdot \vec{E}(t)$, where $\vec{\mu}$ is the transition dipole vector and $\vec{E}(t)$ is the linearly polarized electric field. Throughout this work, the form of the laser pulse with central angular frequency ω is considered as

$$\vec{E}(t) = \tfrac{1}{2}\varepsilon(t)e^{-i\omega t}\vec{e}_{\rm pol} + \tfrac{1}{2}\varepsilon^*(t)e^{i\omega t}\vec{e}_{\rm pol}, \tag{1}$$

where $\vec{e}_{\rm pol}$ is the polarization vector pointing in the z direction and the complex quantity $\varepsilon(t)$ and its complex conjugate $\varepsilon^*(t)$ include the electric field amplitude ε_0, the envelope function $g(t)$, and the phase of the field $\phi(t)$,

$$\varepsilon(t) = \varepsilon_0 g(t) e^{i\phi(t)/2}, \tag{2a}$$

$$\varepsilon^*(t) = \varepsilon_0 g(t) e^{-i\phi(t)/2}. \tag{2b}$$

In the total time-dependent wave function of the system both the essential and nonessential states are explicitly included and it reads [76]

$$\Psi(t) = c_g(t)|g\rangle e^{-i\omega_g t} + c_e(t)|e\rangle e^{-i\omega_e t} + \sum_m c_m(t)|m\rangle e^{-i\omega_m t}. \tag{3}$$

In Eq. (3) the ground and excited states ($3s$ and $4s$ in the case of Na) are denoted by $|g\rangle$ and $|e\rangle$, respectively, while the off-resonant nonessential states are labeled by $|m\rangle$. The $|m\rangle$ states are dipole coupled to $|g\rangle$ and $|e\rangle$ but as they are far from resonance, their population is negligible during the atom-field interaction. The impact of these states on the studied two-photon transition is crucial as they give rise to the dynamic Stark shifts of the $3s$ and $4s$ levels to be discussed below. We note that the m-state manifold consists of p states ($l = 1$) in the present case due to the selection rules for the angular momentum.

After inserting Eq. (3) into the time-dependent Schrödinger equation $i\dot{\Psi} = [H_0 + V(t)]\Psi$ we arrive at the full set of cou-

pled differential equations for the $c_j(t)$ complex amplitudes

$$i\dot{c}_j(t) = \sum\!\!\!\!\!\!\int_k c_k(t)e^{-i\omega_{kj}t}V_{jk}(t), \tag{4}$$

where $\omega_{kj} = \omega_k - \omega_j$ $(j,k = g,e,m)$ and the light-matter interaction term is written as $V_{jk}(t) = -E(t)\mu_{jk}$, with $\mu_{jk} = \langle j|z|k\rangle$ the transition dipole moment (TDM) matrix element between the corresponding eigenstates of the atom. Equation (4) can be greatly simplified by invoking that the μ_{ge} and $\mu_{mm'}$ TDMs are inherently zero. After applying these considerations, Eq. (4) is written as

$$i\dot{c}_g(t) = \sum\!\!\!\!\!\!\int_m c_m(t)e^{i\omega_{gm}t}V_{gm}(t), \tag{5a}$$

$$i\dot{c}_e(t) = \sum\!\!\!\!\!\!\int_m c_m(t)e^{i\omega_{em}t}V_{em}(t), \tag{5b}$$

$$i\dot{c}_m(t) = c_g(t)e^{-i\omega_{gm}t}V_{mg}(t) + c_e(t)e^{-i\omega_{em}t}V_{me}(t). \tag{5c}$$

To reveal the overall impact of the nonessential m-state manifold, we turn to Eq. (5c). As the off-resonant intermediate states rapidly oscillate, the time evolution of the $c_m(t)$ amplitudes can be obtained by adiabatic elimination [77]. After integrating Eq. (5c) by parts and omitting small terms, we arrive at an explicit expression for the $c_m(t)$ amplitudes

$$c_m(t) = \frac{\mu_{mg}}{2}c_g(t)\left[\frac{\varepsilon(t)e^{-i(\omega_{gm}+\omega)t}}{\omega_{mg}-\omega} + \frac{\varepsilon(t)^*e^{-i(\omega_{gm}-\omega)t}}{\omega_{mg}+\omega}\right] + \frac{\mu_{me}}{2}c_e(t)\left[\frac{\varepsilon(t)e^{-i(\omega_{em}+\omega)t}}{\omega_{me}-\omega} + \frac{\varepsilon(t)^*e^{-i(\omega_{em}-\omega)t}}{\omega_{me}+\omega}\right], \tag{6}$$

which is valid as long as the detuning of the $|m\rangle$ states is large compared to the pulse bandwidth, the two-photon detuning, and the Stark shifts of interest. Inserting Eq. (6) into Eqs. (5a) and (5b), the coupled equations

$$i\dot{c}_g(t) = -\sum_m\left\{\frac{|\mu_{mg}|^2}{4}c_g(t)\left[\frac{\varepsilon(t)^2e^{-2i\omega t}+|\varepsilon(t)|^2}{\omega_{mg}-\omega} + \frac{\varepsilon(t)^{*2}e^{2i\omega t}+|\varepsilon(t)|^2}{\omega_{mg}+\omega}\right] + \frac{\mu_{em}\mu_{mg}}{4}c_e(t)\left[\frac{\varepsilon(t)^2e^{-i(4\omega-\Delta)t}+|\varepsilon(t)|^2e^{-i(2\omega-\Delta)t}}{\omega_{me}-\omega} + \frac{\varepsilon(t)^{*2}e^{i\Delta t}+|\varepsilon(t)|^2e^{-i(2\omega-\Delta)t}}{\omega_{me}+\omega}\right]\right\}, \tag{7}$$

$$i\dot{c}_e(t) = -\sum_m\left\{\frac{|\mu_{me}|^2}{4}c_e(t)\left[\frac{\varepsilon(t)^2e^{-2i\omega t}+|\varepsilon(t)|^2}{\omega_{me}-\omega} + \frac{\varepsilon(t)^{*2}e^{2i\omega t}+|\varepsilon(t)|^2}{\omega_{me}+\omega}\right] + \frac{\mu_{em}\mu_{mg}}{4}c_g(t)\left[\frac{\varepsilon(t)^2e^{-i\Delta t}+|\varepsilon(t)|^2e^{-i(\Delta-2\omega)t}}{\omega_{mg}-\omega} + \frac{\varepsilon(t)^{*2}e^{-i(\Delta-4\omega)t}+|\varepsilon(t)|^2e^{-i(\Delta-2\omega)t}}{\omega_{mg}+\omega}\right]\right\} \tag{8}$$

are found, where $\Delta = 2\omega - \omega_{eg}$ is the two-photon detuning. Applying the two-photon RWA, that is, dropping terms that oscillate faster than Δ, the two-state equation

$$i\begin{pmatrix}\dot{c}_g(t)\\ \dot{c}_e(t)\end{pmatrix} = \begin{pmatrix}S_g(t) & \Omega(t)e^{i(\Delta t-\phi(t))}\\ \Omega(t)e^{-i(\Delta t-\phi(t))} & S_e(t)\end{pmatrix}\begin{pmatrix}c_g(t)\\ c_e(t)\end{pmatrix} \tag{9}$$

is obtained, where $\Omega(t)$ is the two-photon Rabi frequency (assumed real)

$$\Omega(t) = -\sum\!\!\!\!\!\!\int_m \frac{\mu_{em}\mu_{mg}}{4}\frac{\varepsilon_0^2 g(t)^2}{\omega_{mg}-\omega} = \Omega_0\varepsilon_0^2 g(t)^2 \tag{10}$$

and $S_k(t)$ is the dynamic Stark shift of the kth level $(k = g,e)$ originating from the nonessential m-state manifold

$$S_k(t) = -\sum\!\!\!\!\!\!\int_m \frac{|\mu_{km}|^2\varepsilon_0^2 g(t)^2}{2}\frac{\omega_{mk}}{\omega_{mk}^2-\omega^2} = S_k^0\varepsilon_0^2 g(t)^2. \tag{11}$$

We note here that both $\Omega(t)$ and $S_k(t)$ follow the $\varepsilon_0^2 g(t)^2$ intensity profile of the pulse in accordance with previous studies [46,51].

It is convenient to transform Eq. (9) into the interaction picture for later purposes, according to the well-known formulas $H' = UHU^\dagger + i\hbar\dot{U}U^\dagger$ and $\Psi' = U\Psi$. Applying the unitary transformation matrix (which leaves the populations unchanged)

$$U = \begin{pmatrix}\exp[i\int_{-\infty}^t S_g(t')dt'] & 0\\ 0 & \exp[i\int_{-\infty}^t S_e(t')dt']\end{pmatrix}, \tag{12}$$

we obtain the equation for the new coefficients

$$i\begin{pmatrix}\dot{a}_g(t)\\ \dot{a}_e(t)\end{pmatrix} = \begin{pmatrix}0 & \Omega(t)e^{i\kappa(t)}\\ \Omega(t)e^{-i\kappa(t)} & 0\end{pmatrix}\begin{pmatrix}a_g(t)\\ a_e(t)\end{pmatrix}, \tag{13}$$

where the $\kappa(t)$ atom-field phase has been introduced using the relative DSS $\delta S(t) = S_e(t) - S_g(t)$ and its negative integral $\gamma(t) = -\int_{-\infty}^t \delta S(t')dt'$,

$$\kappa(t) = -\int_{-\infty}^t \delta S(t')dt' + \Delta t - \phi(t). \tag{14}$$

Modulating the $\phi(t)$ field phase such that $\kappa(t)$ remains constant during the atom-field interaction was found to be a key technique to efficiently transfer population in strong laser fields [47]. This phase-locking technique is equivalent to maintaining the resonance condition at each moment of time during the action of the frequency chirped laser pulse despite the movement of the atomic levels.

In this work, based on the idea of reverse engineering presented by Golubev and Kuleff [25], we aim to derive optimal pulse shapes that compensate for the relative dynamic Stark shift and efficiently control the population dynamics between two strongly coupled states. For that purpose, we will first

predefine the desired evolution pathway of the system and then solve the TDSE (13) inversely for the field. The obtained analytical pulse will be then tested and applied to the Na atom by solving its full TDSE accurately. The main steps of the proposed reverse engineering procedure are detailed in the next section.

III. PULSE REVERSE ENGINEERING

In what follows, we outline the main steps of the reverse engineering procedure applied in this work to obtain an analytical pulse expression for control purposes. Our starting point is the Schrödinger equation of the effective two-level system presented at the end of the preceding section [Eq. (13)]. Making use of Eqs. (2a), (2b), (10), and (14), we can write Eq. (13) as

$$i\dot{a}_g(t) = \Omega_0 \varepsilon^*(t)^2 e^{i\gamma(t)} e^{i\Delta t} a_e(t), \tag{15a}$$

$$i\dot{a}_e(t) = \Omega_0 \varepsilon(t)^2 e^{-i\gamma(t)} e^{-i\Delta t} a_g(t). \tag{15b}$$

These equations are usually solved for fixed parameter values of the external electric field to obtain the time evolution of the system. Our aim in this work is the opposite. After predefining the desired quantum path of the system, we aim to solve Eqs. (15a) and (15b) for the external laser pulse that induces the prescribed time evolution. To do so, we express $\varepsilon^*(t)$ from Eq. (15a) and $\varepsilon(t)$ from Eq. (15b) and then substitute them into the general form of the field presented in Eq. (1),

$$E(t) = \frac{1}{2}\left\{\sqrt{i\frac{\dot{a}_g(t)}{a_e(t)}\frac{1}{\Omega_0}}\exp\left[i\left(\frac{\omega_{eg}}{2}t - \frac{\gamma(t)}{2}\right)\right] + \sqrt{i\frac{\dot{a}_e(t)}{a_g(t)}\frac{1}{\Omega_0}}\exp\left[-i\left(\frac{\omega_{eg}}{2}t - \frac{\gamma(t)}{2}\right)\right]\right\}. \tag{16}$$

The $a_g(t)$ and $a_e(t)$ population amplitudes are complex functions, so they can be written as

$$a_k(t) = \tilde{a}_k(t) e^{i\varphi_k(t)} \quad (k = g, e), \tag{17}$$

where the $\tilde{a}_k(t)$'s are real non-negative functions. In the most general case, the $\varphi_k(t)$ phases can be time dependent [28]. As we will see below, this would lead to additional frequency chirping of the pulse, allowing one to control not only the populations but also the phases of the system. Inserting the above $a_k(t)$'s into Eq. (16), we have

$$E(t) = \frac{1}{2}\left\{\sqrt{\frac{i}{\Omega_0}\frac{\dot{\tilde{a}}_g(t) + i\tilde{a}_g(t)\dot{\varphi}_g(t)}{\tilde{a}_e(t)}}\exp\left[i\left(\frac{\omega_{eg}}{2}t - \frac{\gamma(t)}{2} + \frac{\varphi(t)}{2}\right)\right] + \sqrt{\frac{i}{\Omega_0}\frac{\dot{\tilde{a}}_e(t) + i\tilde{a}_e(t)\dot{\varphi}_e(t)}{\tilde{a}_g(t)}}\exp\left[-i\left(\frac{\omega_{eg}}{2}t - \frac{\gamma(t)}{2} + \frac{\varphi(t)}{2}\right)\right]\right\}, \tag{18}$$

where the $\varphi(t) = \varphi_g(t) - \varphi_e(t)$ relative phase between $a_g(t)$ and $a_e(t)$ has been introduced. We want the ground-state population to evolve according to a continuous function $\eta(t)$, namely, $|\tilde{a}_g(t)|^2 = \eta(t)$. In this case the excited-state population is obtained by $|\tilde{a}_e(t)|^2 = 1 - \eta(t)$. With this convention the absolute values of the complex amplitudes are then given by

$$\tilde{a}_g(t) = \sqrt{\eta(t)}, \tag{19a}$$

$$\tilde{a}_e(t) = \sqrt{1 - \eta(t)}. \tag{19b}$$

Substituting these $\tilde{a}_k(t)$'s into Eq. (18), we get

$$E(t) = \frac{1}{2}\left\{\sqrt{i\frac{\frac{1}{2}\dot{\eta}(t)}{\sqrt{\eta(t)[1-\eta(t)]}}\frac{1}{\Omega_0} - \dot{\varphi}_g(t)\sqrt{\frac{\eta(t)}{1-\eta(t)}}\frac{1}{\Omega_0}} \times \exp\left[i\left(\frac{\omega_{eg}}{2}t - \frac{\gamma(t)}{2} + \frac{\varphi(t)}{2}\right)\right] + \sqrt{i\frac{-\frac{1}{2}\dot{\eta}(t)}{\sqrt{\eta(t)[1-\eta(t)]}}\frac{1}{\Omega_0} - \dot{\varphi}_e(t)\sqrt{\frac{1-\eta(t)}{\eta(t)}}\frac{1}{\Omega_0}} \times \exp\left[-i\left(\frac{\omega_{eg}}{2}t - \frac{\gamma(t)}{2} + \frac{\varphi(t)}{2}\right)\right]\right\}, \tag{20}$$

which can be written in a more convenient form

$$E(t) = \frac{1}{2}\left\{\sqrt[4]{\frac{\frac{1}{4}[\dot{\eta}(t)]^2}{\eta(t)[1-\eta(t)]}\frac{1}{\Omega_0^2} + [\dot{\varphi}_g(t)]^2\frac{\eta(t)}{1-\eta(t)}\frac{1}{\Omega_0^2}} \times \exp\left[i\left(\frac{\omega_{eg}}{2}t - \frac{\gamma(t)}{2} + \frac{\varphi(t)}{2} + \frac{\beta(t)}{2}\right)\right] + \sqrt[4]{\frac{\frac{1}{4}[\dot{\eta}(t)]^2}{\eta(t)[1-\eta(t)]}\frac{1}{\Omega_0^2} + [\dot{\varphi}_e(t)]^2\frac{1-\eta(t)}{\eta(t)}\frac{1}{\Omega_0^2}} \times \exp\left[-i\left(\frac{\omega_{eg}}{2}t - \frac{\gamma(t)}{2} + \frac{\varphi(t)}{2} + \frac{\beta(t)}{2}\right)\right]\right\}, \tag{21}$$

with the $\beta(t)$ function given as

$$\beta(t) = \arctan\left(\frac{-\frac{1}{2}\dot{\eta}(t)}{\eta(t)\dot{\varphi}_g(t)}\right) = \arctan\left(\frac{-\frac{1}{2}\dot{\eta}(t)}{[1-\eta(t)]\dot{\varphi}_e(t)}\right). \tag{22}$$

Equation (21) gives us a real-valued sinusoid function only if the relation

$$\dot{\varphi}_g(t) = \frac{1-\eta(t)}{\eta(t)}\dot{\varphi}_e(t) \tag{23}$$

is satisfied by the $\varphi_g(t)$ and $\varphi_e(t)$ phases or, equivalently, the time evolution of the excited state phase is given by the indefinite integral up to addition by a constant

$$\varphi_e(t) = \int \frac{\eta(t)}{1-\eta(t)}\dot{\varphi}_g(t)dt. \tag{24}$$

Inserting the phase relations (22)–(24) into Eq. (21), we finally obtain the general expression for the laser pulse

$$E(t) = \sqrt[4]{\frac{\frac{1}{4}[\dot{\eta}(t)]^2}{\eta(t)[1-\eta(t)]}\frac{1}{\Omega_0^2} + [\dot{\varphi}_g(t)]^2\frac{\eta(t)}{1-\eta(t)}\frac{1}{\Omega_0^2}} \times \cos\left\{\frac{\omega_{eg}}{2}t + \frac{1}{2}\int_{-\infty}^{t}\delta S(t')dt' + \frac{1}{2}\varphi_g(t) - \frac{1}{2}\int_{-\infty}^{t}\frac{\eta(t')}{1-\eta(t')}\dot{\varphi}_g(t')dt' + \frac{1}{2}\arctan\left(\frac{-\frac{1}{2}\dot{\eta}(t)}{\eta(t)\dot{\varphi}_g(t)}\right)\right\}. \tag{25}$$

The frequency-modulated laser pulse in Eq. (25) drives the strongly coupled dynamically shifted system along a prescribed quantum pathway defined by the $\eta(t)$ and $\varphi_g(t)$ ground-state control functions. Meanwhile, the excited-state population and phase evolutions are dictated by Eqs. (19b) and (24), respectively. The laser pulse in Eq. (25) is very similar to that found recently for one-photon transitions [28] and can be considered a natural extension to strong-field two-photon transitions where dynamic atomic level shifts become relevant. It is important to note here that the relative dynamic Stark shift $\delta S(t')$ in the argument of the cosine function follows the temporal intensity profile of the pulse [see Eq. (11)] and therefore depends on the $\eta(t)$ and $\varphi_g(t)$ control functions.

To proceed further let us specify the actual form of the control functions. Since we are interested in the control of the state populations, let us concentrate on the solution for time-independent phases [25]. In this case, the very general form of the laser pulse in Eq. (25) is greatly simplified. Upon setting $\dot{\varphi}_k(t) = 0$, only the first term survives in the amplitude function; furthermore, in the argument of the cosine function $\varphi(t) \to \varphi = \varphi_g - \varphi_e$ and $\beta(t) \to \pm\frac{\pi}{2}$, depending of the sign of $\dot{\eta}(t)$. As a result, the frequency modulation is merely caused by the $\delta S(t')$ relative DSS term and the only function to be specified is $\eta(t)$. Let us choose the form of $\eta(t)$ such that an arbitrary initial ground-state population $p^i = |a_g(t=-\infty)|^2$ is smoothly connected with a given final ground-state population $p^f = |a_g(t=\infty)|^2$,

$$\eta(t) = \frac{p^i e^{-\alpha t} + p^f}{1 + e^{-\alpha t}}, \tag{26}$$

where the parameter $\alpha > 0$ dictates the rate of change in the populations around $t = 0$. An important boundary condition for the control functions in the presently developed scheme is the disappearance of the time derivative at the beginning and at the end of the control process. The population control function presented above fulfills this condition, namely, $\lim_{t\to\pm\infty}\dot{\eta}(t) = 0$. Inserting the above function $\eta(t)$ into Eq. (25), we arrive at the final form of the engineered laser pulse, which can be considered the main result of this work,

$$E(t) = \sqrt{\frac{\frac{1}{2}\alpha e^{\alpha t}|p^f - p^i|(e^{\alpha t}+1)^{-1}}{|\Omega_0|\sqrt{[p^i + p^f e^{\alpha t}][(1-p^i)+(1-p^f)e^{\alpha t}]}}}\cos\left\{\frac{\omega_{eg}}{2}t - \frac{\frac{1}{4}|p^f - p^i|\left(S_e^0 - S_g^0\right)}{|\Omega_0|(p^f - p^i)}\left[-\arctan\left(\frac{1-2p^i}{2\sqrt{p^i(1-p^i)}}\right) + \arctan\left(\frac{(1-2p^i)+(1-2p^f)e^{\alpha t}}{2\sqrt{[p^i + p^f e^{\alpha t}][(1-p^i)+(1-p^f)e^{\alpha t}]}}\right)\right] + \frac{1}{2}\varphi \pm \frac{\pi}{4}\right\}. \tag{27}$$

En route to Eq. (27), the integration of the relative DSS term in the argument of the cosine function has been carried out according to $\int_{-\infty}^{t}\delta S(t')dt' = \int_{-\infty}^{t}(S_e^0 - S_g^0)|\varepsilon(t')|^2dt'$, making use of the engineered temporal intensity profile $|\varepsilon(t)|^2$ [the term under the big square root in the amplitude function in Eq. (27)]. In the argument of Eq. (27), $+\frac{\pi}{4}$ applies when Ω_0 and $\dot{\eta}(t)$ have the same sign, while $-\frac{\pi}{4}$ corresponds to the opposite case. Throughout the paper, $\varphi = 0$ is applied. The instantaneous time-dependent angular frequency of the engineered laser pulse in Eq. (27) is obtained as the time derivative of the argument of the cosine function

$$\omega(t) = \frac{\omega_{eg}}{2} + \frac{\frac{1}{4}\alpha e^{\alpha t}\left(S_e^0 - S_g^0\right)|p^f - p^i|(e^{\alpha t}+1)^{-1}}{|\Omega_0|\sqrt{[p^i + p^f e^{\alpha t}][(1-p^i)+(1-p^f)e^{\alpha t}]}}. \tag{28}$$

Equation (27) represents a frequency-modulated laser pulse that couples resonantly the dynamically shifted atomic levels at each moment of time. As a result, population is efficiently transferred between the atomic states and the system is driven from an arbitrary initial superposition ($p^i : 1 - p^i$) to a desired final population distribution ($p^f : 1 - p^f$), while the rate of transition is controlled by the parameter α. Compensating for the dynamic Stark shift has been found to be a key technique in controlling strong-field transitions and in this sense our phase-modulated electric field [Eq. (27)] is in agreement with previous results in the field [17,46,51].

IV. TIME PROPAGATION METHODS

To test the validity of the above-presented reverse engineering technique, in the next section we will numerically solve the TDSE in the single-active-electron picture, which has been successfully applied in several strong-field simulations [78–82]. Two completely different methods will be utilized and compared to each other, which are detailed below.

A. Expansion coefficient propagation (TDEC)

The first method is based on the expansion of the total time-dependent wave packet of the active electron in the basis of field-free atomic states [see Eq. (3)]. In this case the TDSE is written as a set of first-order coupled differential equations for the $c_k(t)$ expansion coefficients [Eq. (4)], the solution of which is carried out with the eighth-order Runge-Kutta method in the space of 67 relevant field-free bound

electronic states with $n < 17$ and $l < 5$ principal and angular momentum quantum numbers, respectively. To solve Eq. (4), besides the eigenenergies, the eigenfunctions of Na are required for the determination of the transition dipole moments. These quantities are obtained by the direct diagonalization of the single-active-electron Hamiltonian of Na [65], discretized on a finite-element discrete-variable representation grid. We note that excellent agreement is found with the previously published energy, TDM, and dipole polarizability values for Na [83–85]. The time-dependent populations of the different electronic states are calculated as $p_k(t) = |c_k(t)|^2$ and a proper convergence of the numerical calculations is ensured.

B. Direct wave-packet propagation (TDWP)

The second approach is the *ab initio* solution of the Schrödinger equation. For this purpose we have developed a general framework able to propagate TDSE-like initial-value problems. The code is written in PYTHON and relies heavily on the PETSc program package [86,87] for the representation of the data structures (operator matrices and wave functions) and for the numerically intensive operations on them. SLEPc [87,88] is used to obtain the desired eigenvalues and eigenvectors of operators. For multidimensional problems both the wave functions and the operators are constructed as tensor products of one-dimensional factors.

In the present investigation, we solve the TDSE of the single active electron of Na in spherical coordinates within the dipole approximation

$$i\dot{\Psi}(\vec{r},t) = [-\Delta/2 + V_{\rm core}(r) + E(t)z]\Psi(\vec{r},t) \tag{29}$$

with a Hellmann pseudopotential [89]

$$V_{\rm core}(r) = -\frac{1}{r} + \frac{A}{r}e^{-ar}, \tag{30}$$

which provides the correct ionization potential ($A = 21$ and $a = 2.549\,20$ [65]). The discretization of the problem is achieved with the time-dependent close-coupling method [90]. Considering the axial symmetry of the problem when dealing with linearly polarized pulses, the wave function is written as a partial wave expansion in terms of spherical harmonics with $m = 0$, i.e., the Legendre polynomials $[Y_l^{m=0}(\theta,\varphi) = P_l(\theta)]$ as

$$\Psi(\vec{r},t) = \sum_{l=0}^{l_{\rm max}} \frac{R_l(r,t)}{r} P_l(\theta). \tag{31}$$

Substituting this wave function into the time-dependent Schrödinger equation (29), we obtain a set of coupled differential equations for the radial functions R_l,

$$\begin{aligned} i\frac{\partial R_l(r,t)}{\partial t} = &\left(-\frac{\partial^2}{2\partial r^2} + \frac{l(l+1)}{2r^2} + V_{\rm core}(r)\right)R_l(r,t) \\ &+ E(t)r\left[\sqrt{\frac{(l+1)^2}{(2l+1)(2l+3)}}R_{l+1}(r,t)\right. \\ &\left.+\sqrt{\frac{l^2}{(2l-1)(2l+1)}}R_{l-1}(r,t)\right]. \end{aligned} \tag{32}$$

The radial coordinate is treated in our implementation with the finite-element (FE) discrete-variable representation (DVR) method [91]. In this approach, functions are expanded in terms of linearly independent local basis functions $f_m^{(i)}(r)$ ($f_m^{(i)}(r) = 0 \quad \text{for } r \notin [r^{(i)}, r^{(i+1)}]$, $i = 1,\ldots,N$, and $m = 1,\ldots,n$) defined on variable-length finite elements defined by a set of nodes $r^{(i)}$ $0 \leqslant r^{(1)} < r^{(2)} < \cdots < r^{(N)}$. Our DVR basis consists of Lagrange interpolating polynomials

$$f_m^{(i)}(r) = \prod_{l\neq m} \frac{r - r_l^{(i)}}{r_m^{(i)} - r_l^{(i)}}, \quad r_1^{(i)} \leqslant r \leqslant r_n^{(i)} \tag{33}$$

defined on a Gauss-Lobatto quadrature grid $r_m^{(i)}$ with weights $w_m^{(i)}$. In this quadrature the first and last grid points are chosen to coincide with the interval boundaries, which is crucial to ensure the continuity of the wave function. This is achieved by combining the two basis functions $f_N^{(i)}$ and $f_1^{(i+1)}$ into a single bridge function to finally arrive at the orthonormalized basis

$$\chi_m^{(i)}(r) \equiv \begin{cases} \left[f_n^{(i-1)}(r) + f_1^{(i)}(r)\right]\Big/\sqrt{w_n^{(i-1)} + w_1^{(i)}}, & m = 1 \\ f_m^{(i)}(r)/\sqrt{w_m^{(i)}}, & m = 2,\ldots,n-1 \\ \left[f_n^{(i)}(r) + f_1^{(i+1)}(r)\right]\Big/\sqrt{w_n^{(i)} + w_1^{(i+1)}}, & m = n. \end{cases} \tag{34}$$

The advantage of the FE-DVR method is that any local operator has a diagonal form, and due to the local nature of the basis functions, the derivative and kinetic energy operators have a sparse block-diagonal form, which makes the numerical solution of Eq. (29) fast. In the present calculations the radial grid ranges from 0 to 1100 a.u. over 550 equal length finite elements, with 11 DVR points on each. Given the properties of the dynamics, i.e., the dominance of the $3s$ and $4s$ states and negligible ionization, the Legendre polynomial basis is kept fairly small with $l_{\rm max} = 10$. Convergence according to all numerical parameters is ensured.

The solution of Eq. (29) entails the consecutive application of the short-time propagator

$$\Psi(t + \Delta t) = U(t, t + \Delta t)\Psi(t), \tag{35}$$

where the evolution operator is

$$U(t, t + \Delta t) = e^{-iH(t)\Delta t}. \tag{36}$$

As the above matrix exponent has to be recomputed at each time step, the straightforward application of this evolution operator is impractical. The core idea of the Lanczos algorithm [92] is to perform the time stepping in a Krylov subspace constructed by the repeated application of the Hamiltonian

on the wave function. The matrix representation of Hermitian operators (Lanczos algorithm) in the Krylov subspace is tridiagonal, while that of non-Hermitian operators (Arnoldi algorithm) is upper Hessenberg. In either case, the Krylov space Hamiltonian is a small (typically smaller than 20×20) matrix, so its diagonalization is inexpensive. Most of the numerical effort is required for the construction of the Krylov subspace.

Although the Lanczos propagator is unconditionally stable, it is plagued by the stiffness problem as any other time stepping algorithm. This means that excessively small time steps are needed to reach convergence when high energies are present in the spectrum of the Hamiltonian. The maximal eigenvalue increases rapidly with the increase of angular momenta, which are necessary when dealing with high-intensity long-wavelength radiations. We choose to employ the split-Lanczos [93] algorithm to overcome this difficulty. Its strategy is to factor out the $V_c = l(l+1)/2r^2$ centrifugal potential from the Hamiltonian of Eq. (32),

$$H(t) = H_r(t) + V_c, \tag{37}$$

which is the source of the increased stiffness, and rewrite the evolution operator as

$$U(t, t+\Delta t) = e^{-iV_c \Delta t/2} \left\{ \prod_{i=1}^{N_s(t)} e^{-iH_r(t+\Delta t'_{i-1})\Delta t'_i} \right\} \times e^{-iV_c \Delta t/2} + \mathcal{O}(\Delta t^3), \tag{38}$$

where

$$\sum_{i=1}^{N_s(t)} \Delta t'_i = \Delta t, \quad \Delta t'_0 = 0. \tag{39}$$

Since V_c is diagonal, the exponential term containing it can be easily applied to the wave function, while the propagation with H_r is performed with the ordinary Lanczos algorithm with adaptive time step $\Delta t'_i$. The splitting of the Hamiltonian introduces an error proportional to Δt^3 due to the noncommutativity of H_r and V_c. This is however negligible in our calculations, where the overall time step is set to $\Delta t \sim 0.01$ a.u. The size of our Krylov subspace is 8, which means that the number of Lanczos steps within Δt is $N_s(t) \leqslant 3$ throughout the whole propagation.

The population of the different electronic states is obtained upon projecting the propagated wave packet on the given eigenfunction $p_k(t) = |\langle \psi_k | \Psi(t) \rangle|^2$. The ionization yield is calculated as $p_{\text{ion}} = 1 - \sum_k p_k(\infty)$, where k runs over the bound states.

V. RESULTS AND DISCUSSION

Before we apply the engineered laser pulse [Eq. (27)] to steer the $3s \rightarrow 4s$ two-photon transition of Na, let us analyze the control parameter dependence of $E(t)$. As seen in Fig. 2(a), the envelope function of the electric field strength profile $[\varepsilon_0 g(t)]$ is Gaussian-like with a slight asymmetry around the center of transition ($t = 0$). The transition rate parameter α, which controls the speed of transition, basically determines the FWHM pulse duration and the ε_0 electric field strength [see Fig. 2(b)]. Slow transitions (small α) require

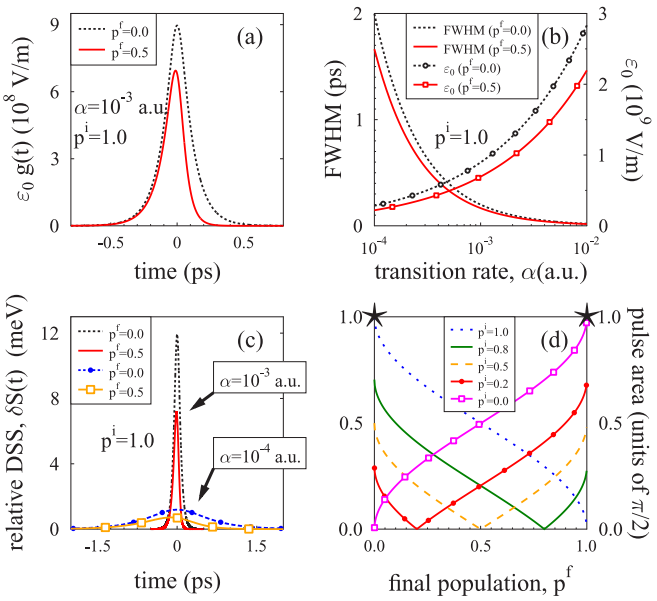

FIG. 2. Control parameter dependence of the engineered laser pulse $E(t)$ [Eq. (27)] applied to atomic Na. (a) The temporal envelope profile $\varepsilon_0 g(t)$ is presented for two different values of the final target population p^f. The larger the desired population change, the stronger and longer the required laser pulse. This is further illustrated in (b), where the FWHM pulse duration and the peak electric field strength ε_0 are shown as a function of transition rate. Fast transitions require strong and short pulses which might lead to the breakdown of $E(t)$ due to the application of AER (see the text for details). (c) Relative dynamic Stark shift that is responsible for the frequency chirping of $E(t)$ is presented for two transition rate values and population variations. (d) Pulse area of $E(t)$ calculated according to Eq. (40). The stars correspond to two-photon π pulses that induce a total population inversion between the $3s$ and $4s$ states.

long pulses of moderate intensity, while for inducing fast transitions (large α), short and intense pulses are needed. Very fast transitions, as will be detailed below, restrict the application of $E(t)$, as the applied approximations (AE plus RWA) can get violated in such an extreme situation.

The frequency modulation of $E(t)$ in Eq. (27) is dictated by the relative DSS of the involved strongly coupled states ($3s$ and $4s$). As the Stark shift of $3s$ is negative, while that of the $4s$ state is positive (see Table I), the relative DSS for the $3s \rightarrow 4s$ transition is positive. The $3s$ and $4s$ states are thus shifted apart from each other, and in that case a positive chirping can maintain resonance at each moment [Fig. 2(c)]. The area of the pulse, calculated as the integral of the two-photon Rabi frequency, making use of the $\varepsilon_0^2 g(t)^2$ engineered temporal intensity profile of $E(t)$,

$$\Theta = \int_{-\infty}^{\infty} |\Omega(t')| dt', \tag{40}$$

is independent of the value of α, but strongly depends on the population variations [see Fig. 2(d)]. In the special case of total population inversion, the pulse area is $\pi/2$, as expected for two-photon π pulses [see the stars in Fig. 2(d)].

In order to apply the control pulse in Eq. (27), several system parameters, such as the bare resonance angular

TABLE I. Peak values of the $3s$ and $4s$ state dynamic Stark shifts [Eq. (11)] and the corresponding two-photon Rabi frequency [Eq. (10)] of Na applied in the present work. The contribution of the different p states is presented up to $n = 16$. The laser frequency is set to exact two-photon resonance for the $3s \rightarrow 4s$ transition ($\omega_{\rm res} = 1.588\,600\,194\,4$ eV). Atomic units are applied.

State	S^0_{3s} (a.u.)	S^0_{4s} (a.u.)	Ω_0 (a.u.)
$3p$	−98.9440612	−69.9490101	86.4315444
$4p$	−0.1989778	120.7626457	−3.9353948
$5p$	−0.0199985	5.8107205	−0.1206079
$6p$	−0.0051263	3.0668374	−0.0229614
$7p$	−0.0020004	−13.5777867	−0.0079140
$8p$	−0.0009846	−0.6559644	−0.0036537
$9p$	−0.0005595	−0.2269416	−0.0020006
$10p$	−0.0003504	−0.1108723	−0.0012234
$11p$	−0.0002350	−0.0640182	−0.0008075
$12p$	−0.0001659	−0.0409204	−0.0005638
$13p$	−0.0001218	−0.0280076	−0.0004105
$14p$	−0.0000924	−0.0201555	−0.0003092
$15p$	−0.0000718	−0.0150563	−0.0002391
$16p$	−0.0000570	−0.0115908	−0.0001891
total	−99.1728026	44.9398798	82.3352695

frequency ω_{4s3s}, the peak Stark shifts S^0_{3s} and S^0_{4s} [Eq. (11)], and the peak Rabi frequency Ω_0 [Eq. (10)], have to be evaluated with the help of the eigenenergies and TDMs of Na. These strong-field parameters are shown in Fig. 3 as a function of the central angular frequency of the laser in the vicinity of the bare two-photon (TP) resonance ($\omega_{\rm res} = \omega_{4s3s}/2$). While Ω_0 and S^0_{3s} behave rather smoothly, the excited-state Stark shift S^0_{4s} exhibits abrupt jumps, which are attributed to higher-lying p states nearly one-photon resonant with $4s$. This is clearly seen in Fig. 3(a) by comparing the blue dashed line and the red solid line: Owing to the $7p$ state, the $4s$ Stark shift is substantially modified in the vicinity of the bare TP resonance energy $\omega_{\rm res}$. The impact of the $7p$ state on the other quantities in Fig. 3 is negligible.

The individual contributions of the different p states to the Stark shifts and Rabi frequency are listed in Table I. Clearly, the nearby $3p$ and $4p$ states give the dominant contributions, while the higher states become less and less important with increasing n. The only exception is the $4s$ Stark shift, which has a notable contribution from the one-photon resonant $7p$ state.

After having all the system parameters necessary for the construction of our control pulse, we are now ready to apply $E(t)$ to drive the $3s \rightarrow 4s$ transition along some user-defined quantum path [specified by the control function $\eta(t)$ in Eq. (26)]. As a concrete example, let us choose $p^i = 1.0$ and $p^f = 0.5$ to drive the system from the initially populated $3s$ state to an equal population distribution of the $3s$ and $4s$ states. The obtained results are shown in Fig. 4 for both large- and small-α values to simulate fast and slow transitions, respectively. Here two completely different methods are applied to solve the Schrödinger equation of the active electron of Na in the presence of the engineered $E(t)$ laser pulse. Importantly, the TDEC results, which are obtained by the propagation of expansion coefficients, are fully supported

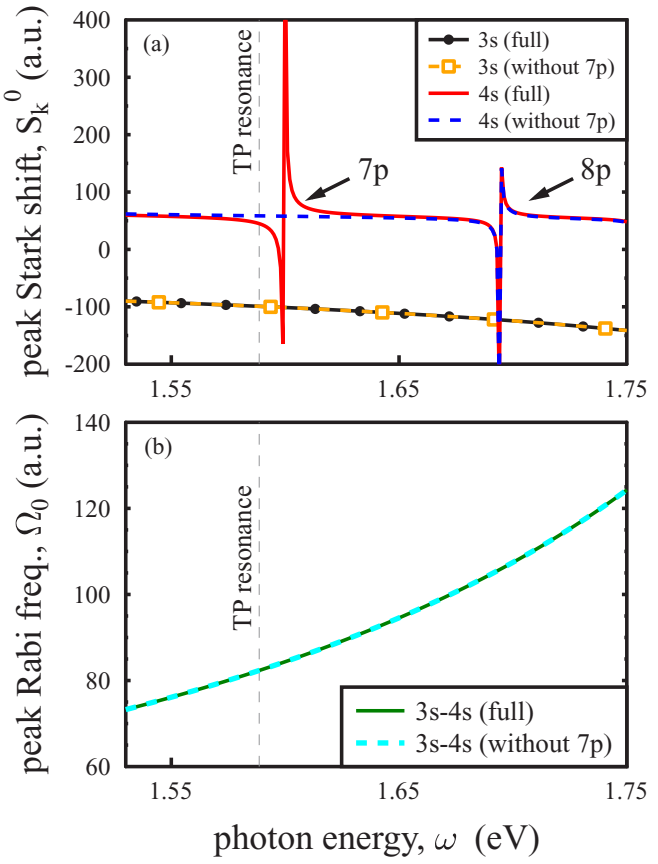

FIG. 3. Strong-field parameters of the $3s \rightarrow 4s$ two-photon transition of atomic sodium. Peak values of the (a) $3s$ and $4s$ state dynamic Stark shifts are calculated according to Eq. (11), while the (b) two-photon Rabi frequency between the $3s$ and $4s$ states is obtained from Eq. (10). The solid lines correspond to full results, which are calculated in the space of 67 electronic states ($n < 17, l < 5$). Quantities denoted by dashed lines are calculated upon exclusion of the one-photon resonant $7p$ state from the description. Owing to the resonant $7p$ state, the $4s$ Stark shift becomes sensitive to small variations of the laser frequency near the two-photon resonance. The vertical dashed line indicates the bare two-photon resonance energy between the strongly coupled $3s$ and $4s$ states ($\omega_{\rm res} = 1.588\,600\,194\,4$ eV).

by the TDWP results, which rely on the direct propagation of the three-dimensional wave packet on a grid (for details, see Sec. IV). The agreement of the two methods is best when the transition is slow. The very slight deviation of the populations in the case of fast transitions is attributed to the small amount of ionization, which is not described by the TDEC method. This is demonstrated in Fig. 4(c) by the ionization yields obtained from the TDWP method for different α's. For slow transitions, the pulse duration is in the picosecond regime and owing to the narrow bandwidth, the system dynamics is confined to the $3s$ and $4s$ states and there is no ionization. However, by increasing α, the intensity and bandwidth of the pulse grow, which can lead to resonance-enhanced ionization first mediated by $7p$ and then involving other bound states as well when α is large.

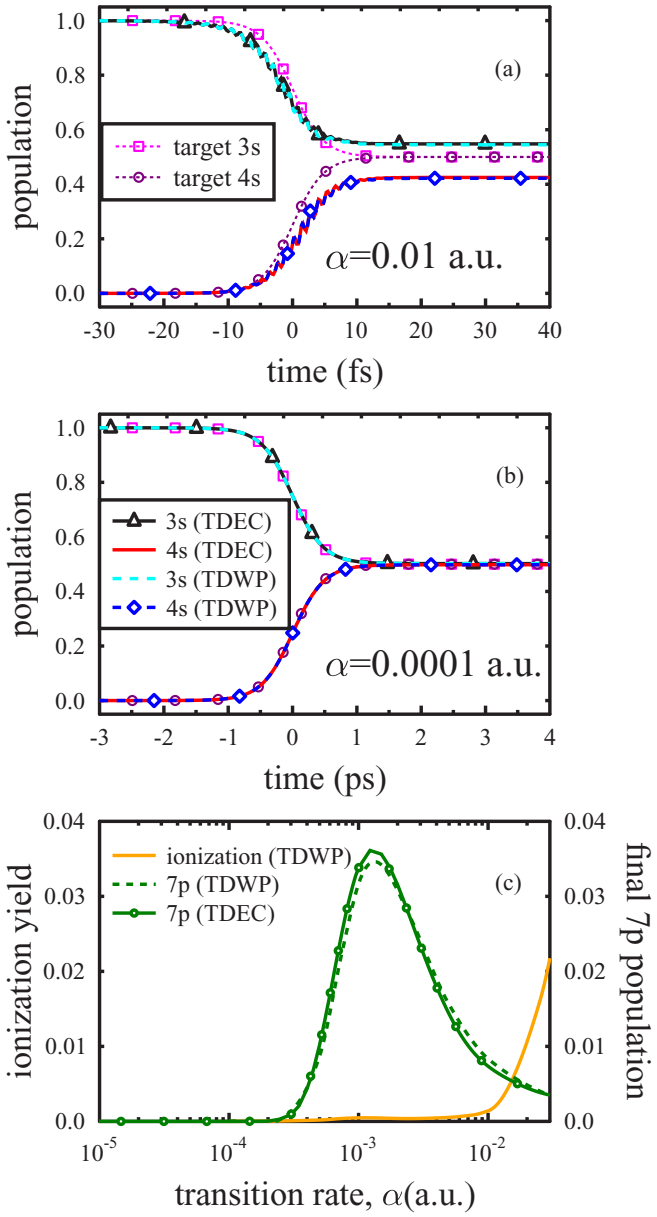

FIG. 4. Comparison of the time-dependent $3s$ and $4s$ state populations calculated with the TDEC and TDWP methods (see Sec. IV). For both (a) fast and (b) slow transitions, the two completely different methods give perfect agreement; furthermore, the simulated population curves follow the analytical target functions (dotted lines with open circles and open squares). (c) The slight increase in the ionization probability around $\alpha = 0.001$ a.u. correlates with the maximum in the final $7p$ populations, indicating that a Stark shifted transient resonance between $4s$ and $7p$ opens up a resonance-enhanced ionization channel.

Another important feature in Fig. 4 is that the population functions obtained from the numerical solution of the TDSE follow the prescribed control functions. Here the agreement is again best when the transition is slow. As described above, for faster transitions the two-level description becomes less accurate since the neighboring states start to get populated. Furthermore, in the case of large α the approximations applied in Sec. II (AE plus RWA) are not perfectly satisfied and the pulse can only approximately drive the system along the user-defined target function.

Based on the general nice agreement of the two different time propagation techniques, in the following we will apply the much faster TDEC method for the exploration of the validity of $E(t)$. In Fig. 5 a detailed survey of our control pulse is presented. Four different population variations are considered corresponding to the four rows of panels. In Figs. 5(a)–5(c) a total population inversion is demonstrated and the population change decreases from the top to the bottom panels. In Figs. 5(a), 5(d), 5(g), and 5(j) the state populations, obtained after the pulse has expired, are presented for different transition rates. For small-α values ($\alpha < 0.0003$ a.u.) the laser pulse is of moderate intensity and rather long (including many optical cycles). Owing to the narrow bandwidth, the neighboring off-resonant states are avoided and the user-defined population control functions are perfectly reached by the driven system [see the horizontal dotted lines with open circles and squares in Figs. 5(a), 5(d), 5(g), and 5(j)]. On the other extremum, when α is large ($\alpha > 0.01$ a.u.) the laser pulse becomes rather strong and short (including only a few cycles). In such a case the AER is violated, the neighboring states become populated, and as a result the system only approximately follows the prescribed control functions. It is important to note here that from the populated neighboring p states a single photon can transfer population not only back to the s states but further to the d manifold too. The population of the g series is however still negligible even for the largest α considered in this work. In the intermediate region (0.0003 a.u.$< \alpha < 0.01$ a.u.), the $7p$ state gets populated by the control pulse (green dotted lines), which prevents the system from perfectly following the desired quantum path. To clarify the role of the $7p$ state, we have solved the TDSE by excluding the $7p$ state from the description. According to the obtained population functions (dashed lines in Fig. 5), much better control is achieved if there is no resonant state present in the vicinity of the controlled states.

To explicitly demonstrate the time evolution of the driven system, we choose two specific α values. In the case of $\alpha = 0.01$ a.u., the transitions occur in the order of 20 fs [Figs. 5(b), 5(e), 5(h), and 5(k)], while for $\alpha = 0.0001$ a.u. in approximately 2 ps. Requiring fast transitions, the system cannot follow the target function exactly as the AER is only partially satisfied. The larger the prescribed population variation, the larger the deviation between the numerically obtained and analytical population functions. However, when the desired transition is sufficiently slow, the system is perfectly driven along the control pathways by $E(t)$ irrespective of the actual values of the population change.

The non-negligible final population of the $7p$ state in the intermediate transition rate region (green dotted lines in Fig. 5) is the result of Stark shifted transient resonance between the $4s$ and $7p$ states. To better illustrate this resonance condition, we calculate the Stark shifted $7p$ state energy and the Stark shifted $4s$ energy dressed by the $\omega(t)$ chirped photon energy as

$$\omega_{4s}(t) = \omega_{4s} + S_{4s}(t) + \omega(t), \tag{41a}$$

$$\omega_{7p}(t) = \omega_{7p} + S_{7p}(t). \tag{41b}$$

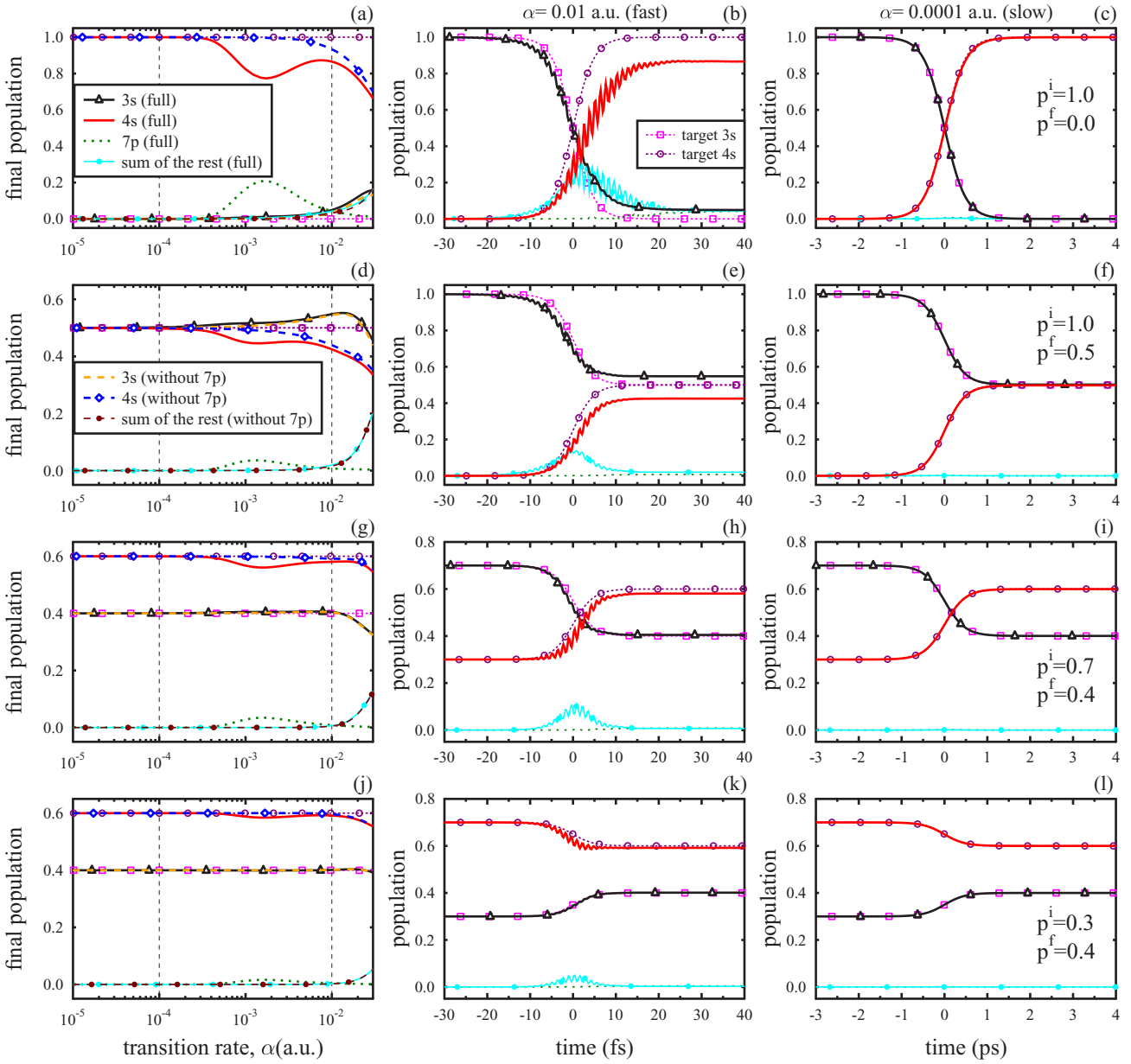

FIG. 5. Application of the engineered laser pulse $E(t)$ [Eq. (27)] to control the population dynamics of the $3s \rightarrow 4s$ two-photon transition in atomic sodium. A wide range of the transition parameter α is considered (left column) to achieve complete control over the rate of transition and the final target $3s$ and $4s$ populations (dotted lines with open circles and squares). The different rows of panels correspond to increasing population modulations from bottom to top. (a)–(c) demonstrate a complete population inversion between the $3s$ and $4s$ states, while (d)–(f) depict an equal final population distribution of these states. Upon fast transitions we only approximately reach the target superpositions (middle column), while applying sufficiently slow transitions, any desired population dynamics is achieved with $E(t)$ (right column) (see the perfect matching of the control functions and the numerically obtained $3s$ and $4s$ populations). The full results are calculated in the space of 67 electronic states ($n < 17, l < 5$) with the TDEC method. Quantities denoted by dashed lines are calculated upon exclusion of the one-photon resonant $7p$ state from the description. Results are obtained by solving Eq. (4) with $E(t)$ in Eq. (27). The vertical dashed lines indicate the specific α values that are applied in the middle and right columns.

In Eqs. (41a) and (41b) the peak Stark shift of the $7p$ state, which is caused by the s ($l = 0$) and d ($l = 2$) state manifolds, is found to be $S^0_{7p} = 68.602\,787$ a.u. Furthermore, the frequency-modulated angular frequency is given in Eq. (28). The energies of the one-photon coupled $4s$ and $7p$ states, calculated at the maximum $t_{\max}$ of the pulse, are shown in Fig. 6 for different transition rate values. In the case of small α, the laser intensity is low; therefore, the individual Stark shifts, as well as the frequency modulation of the field, is rather small. The energetic ordering of the $4s$ and $7p$ states is the same as in the field-free case. By increasing α, the laser gets more and more intense, which leads to the growth of both the Stark shifts and the frequency modulation of $E(t)$. As a result, the energy of the dressed $4s$ state is increasing more rapidly than that of the $7p$ state, leading to the crossing of the two energy curves. As seen in Fig. 6, this crossing of

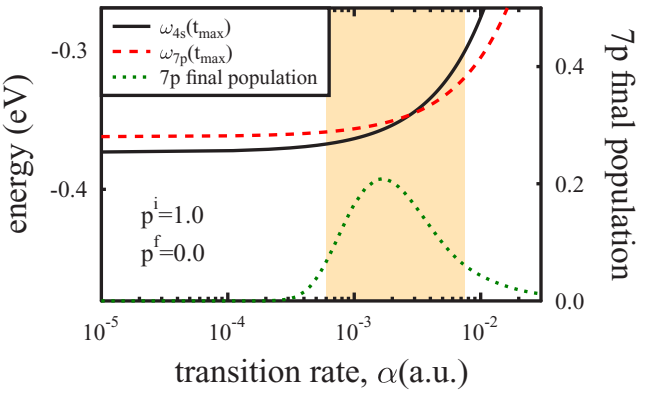

FIG. 6. Energies of the one-photon nearly resonant $4s$ and $7p$ states of Na under the action of the engineered laser pulse given in Eq. (27). The Stark shifted $7p$ state energy (red dashed line) and the Stark shifted $4s$ state energy, dressed by the chirped photon energy $\omega(t_{\max})$ (black solid line) are calculated according to Eqs. (41a) and (41b) for different transition rate values (peak energies are considered at the maximum $t_{\max}$ of the pulse). Upon increasing α (and hence increasing field strength and frequency modulation), these Stark shifted one-photon coupled states form an energy crossing that gives rise to an efficient population transfer from the $4s$ to the $7p$ state [see the shaded region and the final $7p$ populations shown by the green dotted line from Fig. 5(a)].

the $4s$ and $7p$ energy curves occurs right in the intermediate transition rate region (shaded area), allowing for an efficient population transfer to $7p$, seen already in Fig. 5.

Finally, let us inspect how sensitive the laser pulse $E(t)$ is to the imperfections of its parameters. In particular we focus on the system specific parameters, like the peak Rabi frequency Ω_0, the resonance angular frequency $\omega_{\rm res} = \frac{1}{2}\omega_{4s3s}$, and the relative DSS $\delta S(t)$ that is responsible for the frequency modulation of $E(t)$ in Eq. (27). The imperfections of these quantities are defined by the relations

$$\Omega_0' = (1+\delta_\Omega)\Omega_0, \tag{42a}$$

$$\omega_{\rm res}' = (1+\delta_\omega)\omega_{\rm res}, \tag{42b}$$

$$\delta S'(t) = (1+\delta_S)\delta S(t). \tag{42c}$$

Upon varying δ_Ω, δ_ω, and δ_S, one can simulate possible preparation errors occurring, e.g., in an experimental realization of $E(t)$. The obtained results are presented in Fig. 7 for the specific case of $p^i = 0.7$ and $p^f = 0.4$ simulating slow transitions ($\alpha = 0.0001$ a.u.). As can be seen in Figs. 7(a) and 7(b), the final target population value of the $4s$ excited state (0.6) is reached by $E(t)$ in a wide interval of the imperfection parameters. Deviation of the Rabi frequency from its optimal value ($\delta_\Omega = 0$) can be compensated by a proper positive or negative chirping of the control pulse [see the dashed line in Fig. 7(a)]. The same holds when the resonance frequency deviates from its optimal value ($\delta_\omega = 0$), but in this case the chirping of the pulse allows for compensation in a somewhat narrower parameter range [see the dashed line in Fig. 7(b)]. Interestingly, transform-limited (TL) pulses, when there is no frequency modulation at all, can still drive the Stark shifted system close to the desired final state. This is demonstrated by the horizontal dash-dotted lines in Fig. 7; for example,

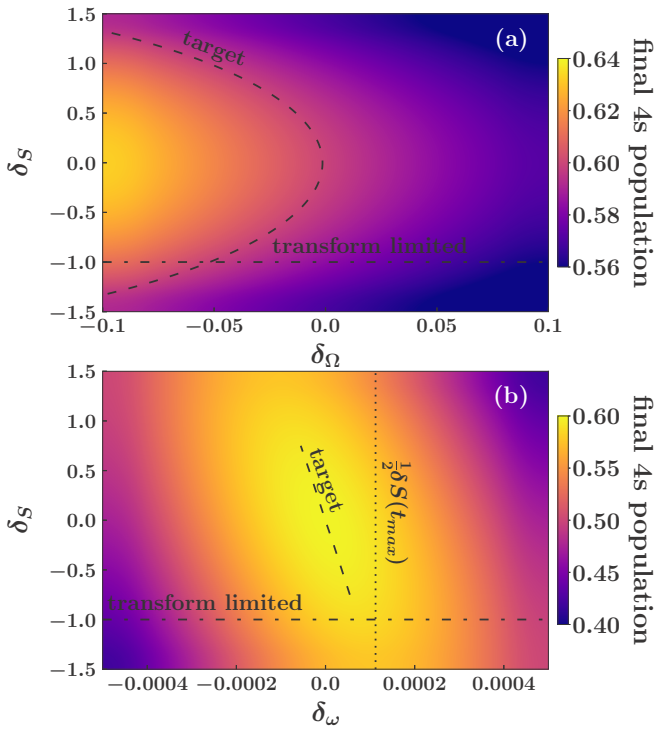

FIG. 7. Final $4s$ state populations of Na as a function of the laser parameter imperfections defined in Eqs. (42a)–(42c). Deviations from the optimal values of (a) the Rabi frequency and (b) the resonance laser frequency lead to a deterioration of the final $4s$ state population from its target value of 0.6. A proper modification of the frequency chirping of the laser pulse can however still maintain the target $4s$ population (see the dashed lines in both panels). The horizontal dash-dotted lines indicate transform-limited (unchirped) pulses, which can still drive the system close to the desired final target state in some cases. The vertical dotted line in (b) indicates the peak relative DSS per photon $\frac{1}{2}\delta S(t_{\max})$. The remaining fixed values of the applied laser pulses are $\alpha = 0.0001$ a.u., $p^i = 0.7$, and $p^f = 0.4$. The presented results are obtained by the TDEC method solving Eq. (4) in the space of 67 electronic states, with $E(t)$ in Eq. (27).

an appropriately positively detuned TL pulse can steer the $4s$ population close to 0.6 in spite of the fact that the dynamic resonance condition is not satisfied. In such a case, the blue-detuned TL pulse, the detuning of which approximately equals 70% of the peak relative DSS per photon [vertical dotted line in Fig. 7(b)], can maintain resonance in a time-averaged sense, which still proves to be efficient. This issue might deserve further investigation in a different paper.

In summary, the reverse engineering scheme presented in this paper allows for the design of analytical laser pulses to drive strong-field transitions along desired pathways. Although exemplified by two-photon transitions, the generalization of the scheme to N-photon transitions is possible [41]. Owing to the applied approximations in the underlying two-state model (the RWA and AE approximation), there exists a lower bound for the operation time of the laser pulse. For the RWA to remain valid, the pulse has to possess at least a few oscillation periods. On the other hand, the AE approximation typically requires a stricter condition: In the

case where there is a nearly single-photon resonant state close to the target states, for a proper operation, the pulse bandwidth has to be smaller than the related single-photon detuning. Handling of the above negative effects, namely, the inhibition of unwanted transitions [9], the avoidance of the RWA [10,21], or even the increase of robustness against different errors [7], has been addressed before in the STA framework. These can provide possible directions for the extension of the presently developed control scheme. The efficiency of our control pulse was demonstrated by the exact solution of the TDSE, and the accurate numerical results obtained for Na are in line with available data in the literature. Our extensive study presented here clearly confirms that dynamic Stark shifts play a fundamental role in strong-field transitions and have to be considered in the frequency modulation of the laser for efficient control.

VI. CONCLUSION

In this paper we have developed a reverse engineering scheme to control the dynamics of strong-field atomic transitions. Considering the $3s \rightarrow 4s$ two-photon transition of atomic sodium as a concrete example, we have designed an analytical laser pulse by solving the TDSE of a two-level effective model in an inverse manner [Eq. (27)]. The envelope function and phase of the engineered laser pulse have been tailored such that the dynamically Stark shifted system is resonantly driven from an arbitrary initial population distribution to a desired final superposition. In contrast to many other works, not only the final target populations, but also the quantum path completed by the system is controlled by the obtained laser pulse.

Solving the TDSE of the single active electron of Na with two completely different methods, i.e., either propagating time-dependent coefficients or propagating the three-dimensional wave packet on a grid, we have verified the validity of the engineered laser pulse (Fig. 4). Upon varying the desired speed of transition (controlled by the parameter α), different regimes have been identified (Fig. 5). For slow transitions ($\alpha < 0.0003$ a.u.), the engineered pulse works the best. In such a case the applied approximations (AER) are well satisfied and the user-defined population control functions are perfectly followed by the driven system. On the other hand, for very fast transitions ($\alpha > 0.01$ a.u.) the field becomes rather intense and short (including a few cycles only). In this case the AER starts to fail and as a result the pulse can only approximately drive the system along the target pathway.

The impact of a single-photon resonant state on the studied two-photon transition, often encountered in alkali metals, has been investigated too. In the intermediate transition rate region (0.0003 a.u.$< \alpha < 0.01$ a.u.) a transient resonance between the Stark shifted $4s$ and $7p$ states has been demonstrated, which opens a resonance-enhanced multiphoton ionization channel and thus leads to a failure of the two-level description. Within the scope of the applied approximations, the engineered laser pulse was found to be surprisingly robust against imperfections of the different system parameters appearing in the expression of the laser pulse, such as the relative Stark shift, the Rabi frequency, and the bare resonance frequency (Fig. 7).

ACKNOWLEDGMENTS

S. Borbély is gratefully acknowledged for valuable discussions. This research was supported by the EU-funded Hungarian Grant No. EFOP-3.6.2-16-2017-00005. The ELI-ALPS Project (No. GINOP-2.3.6-15-2015-00001) is supported by the European Union and co-financed by the European Regional Development Fund.

[1] M. Shapiro and P. Brumer, Adv. At. Mol. Opt. Phys. **42**, 287 (2000).
[2] K. Bergmann, H. Theuer, and B. W. Shore, Rev. Mod. Phys. **70**, 1003 (1998).
[3] N. V. Vitanov, A. A. Rangelov, B. W. Shore, and K. Bergmann, Rev. Mod. Phys. **89**, 015006 (2017).
[4] W. S. Warren, H. Rabitz, and M. Dahleh, Science **259**, 1581 (1993).
[5] D. J. Tannor and S. A. Rice, Adv. Chem. Phys. **70**, 441 (1988).
[6] B. J. Sussman, D. Townsend, M. Y. Ivanov, and A. Stolow, Science **314**, 278 (2006).
[7] A. Ruschhaupt, X. Chen, D. Alonso, and J. G. Muga, New J. Phys. **14**, 093040 (2012).
[8] D. Guéry-Odelin, A. Ruschhaupt, A. Kiely, E. Torrontegui, S. Martínez-Garaot, and J. G. Muga, Rev. Mod. Phys. **91**, 045001 (2019).
[9] A. Kiely and A. Ruschhaupt, J. Phys. B **47**, 115501 (2014).
[10] C. Whitty, A. Kiely, and A. Ruschhaupt, Phys. Rev. Research **2**, 023360 (2020).
[11] Q. Zhang, X. Chen, and D. Guéry-Odelin, Entropy **23**, 84 (2021).
[12] D. Stefanatos and E. Paspalakis, Europhys. Lett. **132**, 60001 (2021).
[13] A. Smponias, D. Stefanatos, and E. Paspalakis, J. Appl. Phys. **129**, 123107 (2021).
[14] I. R. Solá, B. Y. Chang, S. A. Malinovskaya, and V. S. Malinovsky, Adv. At. Mol. Opt. Phys. **67**, 151 (2018).
[15] N. V. Golubev, V. Despré, and A. I. Kuleff, J. Mod. Opt. **64**, 1031 (2017).
[16] T. Propson, B. E. Jackson, J. Koch, Z. Manchester, and D. I. Schuster, arXiv:2103.15716.
[17] S. Zou, Q. Ren, G. G. Balint-Kurti, and F. R. Manby, Phys. Rev. Lett. **96**, 243003 (2006).
[18] S. Zou, C. Sanz, and G. G. Balint-Kurti, J. Chem. Phys. **129**, 124307 (2008).
[19] Q. Zhang, X. Chen, and D. Guéry-Odelin, Sci. Rep. **7**, 15814 (2017).
[20] X. Chen and J. G. Muga, Phys. Rev. A **86**, 033405 (2012).
[21] S. Ibáñez, Y.-C. Li, X. Chen, and J. G. Muga, Phys. Rev. A **92**, 062136 (2015).
[22] Y.-H. Kang, Y.-H. Chen, B.-H. Huang, J. Song, and Y. Xia, Ann. Phys. (Berlin) **529**, 1700004 (2017).

[23] Y.-H. Kang, B.-H. Huang, P.-M. Lu, and Y. Xia, Laser Phys. Lett. **14**, 025201 (2017).
[24] D. Ran, Z.-C. Shi, J. Song, and Y. Xia, Phys. Rev. A **96**, 033803 (2017).
[25] N. V. Golubev and A. I. Kuleff, Phys. Rev. A **90**, 035401 (2014).
[26] N. V. Golubev and A. I. Kuleff, Phys. Rev. A **91**, 051401(R) (2015).
[27] I. Medina and F. L. Semião, Phys. Rev. A **100**, 012103 (2019).
[28] A. Csehi, J. Phys. B **52**, 195004 (2019).
[29] D. Ran, W.-J. Shan, Z.-C. Shi, Z.-B. Yang, J. Song, and Y. Xia, Phys. Rev. A **101**, 023822 (2020).
[30] D. Ran, B. Zhang, Y.-H. Chen, Z.-C. Shi, Y. Xia, R. Ianconescu, J. Scheuer, and A. Gover, Opt. Lett. **45**, 3597 (2020).
[31] G. Dridi, K. Liu, and S. Guérin, Phys. Rev. Lett. **125**, 250403 (2020).
[32] E. Barnes and S. Das Sarma, Phys. Rev. Lett. **109**, 060401 (2012).
[33] F. Impens and D. Guéry-Odelin, Sci. Rep. **9**, 4048 (2019).
[34] F.-Q. Dou, Z.-M. Yan, and L.-N. Hu, Physica A **533**, 121932 (2019).
[35] D. V. Novitsky, Phys. Rev A **86**, 063835 (2012).
[36] Q.-T. Xie and X.-L. Liu, Chinese Phys. B **29**, 060305 (2020).
[37] J. L. Paz, J. R. León-Torres, L. Lascano, and C. Costa-Vera, Opt. Commun. **405**, 238 (2017).
[38] Z. Sun, C. Wang, W. Zhao, Y. Zheng, and C. Yang, Phys. Chem. Chem. Phys. **20**, 20957 (2018).
[39] N. B. Delone and V. P. Krainov, Phys.—Usp. **42**, 669 (1999).
[40] B. J. Sussman, Am. J. Phys. **79**, 477 (2011).
[41] D. Meshulach and Y. Silberberg, Phys. Rev. A **60**, 1287 (1999).
[42] N. Dudovich, B. Dayan, S. M. Gallagher Faeder, and Y. Silberberg, Phys. Rev. Lett. **86**, 47 (2001).
[43] S. A. Hosseini and D. Goswami, Phys. Rev. A **64**, 033410 (2001).
[44] T. Rickes, L. P. Yatsenko, S. Steuerwald, T. Halfmann, B. W. Shore, N. V. Vitanov, and K. Bergmann, J. Chem. Phys. **113**, 534 (2000).
[45] A. Präkelt, M. Wollenhaupt, C. Sarpe-Tudoran, and T. Baumert, Phys. Rev. A **70**, 063407 (2004).
[46] C. Trallero-Herrero, D. Cardoza, T. C. Weinacht, and J. L. Cohen, Phys. Rev. A **71**, 013423 (2005).
[47] C. Trallero-Herrero, J. L. Cohen, and T. C. Weinacht, Phys. Rev. Lett. **96**, 063603 (2006).
[48] A. Gandman, L. Chuntonov, L. Rybak, and Z. Amitay, Phys. Rev. A **75**, 031401(R) (2007).
[49] M. Haas, U. D. Jentschura, C. H. Keitel, N. Kolachevsky, M. Herrmann, P. Fendel, M. Fischer, T. Udem, R. Holzwarth, T. W. Hänsch, M. O. Scully, and G. S. Agarwal, Phys. Rev. A **73**, 052501 (2006).
[50] B. D. Bruner, H. Suchowski, N. V. Vitanov, and Y. Silberberg, Phys. Rev. A **81**, 063410 (2010).
[51] S. Lee, J. Lim, J. Ahn, V. Hakobyan, and S. Guérin, Phys. Rev. A **82**, 023408 (2010).
[52] S. Lee, J. Lim, C. Y. Park, and J. Ahn, Opt. Express **19**, 2266 (2011).
[53] W. Lee, H. Kim, K. Kim, and J. Ahn, Phys. Rev. A **92**, 033415 (2015).
[54] V. A. Astapenko and S. V. Sakhno, J. Mod. Opt. **63**, 2198 (2016).
[55] M. Fushitani, C.-N. Liu, A. Matsuda, T. Endo, Y. Toida, M. Nagasono, T. Togashi, M. Yabashi, T. Ishikawa, Y. Hikosaka, T. Morishita, and A. Hishikawa, Nat. Photon. **10**, 102 (2016).
[56] T. Nieddu, T. Ray, K. S. Rajasree, R. Roy, and S. N. Chormaic, Opt. Express **27**, 6528 (2019).
[57] Y. Ma, X. Huang, X. Wang, L. Ji, Y. He, L. Qiu, J. Zhao, Y. Wang, and S. Wu, Opt. Express **28**, 17171 (2020).
[58] D. Chetty, R. D. Glover, X. M. Tong, B. A. de Harak, H. Xu, N. Haram, K. Bartschat, A. J. Palmer, A. N. Luiten, P. S. Light, I. V. Litvinyuk, and R. T. Sang, arXiv:2108.06841.
[59] R. R. Freeman, P. H. Bucksbaum, H. Milchberg, S. Darack, D. Schumacher, and M. E. Geusic, Phys. Rev. Lett. **59**, 1092 (1987).
[60] G. N. Gibson, R. R. Freeman, and T. J. McIlrath, Phys. Rev. Lett. **69**, 1904 (1992).
[61] M. Krug, T. Bayer, M. Wollenhaupt, C. Sarpe-Tudoran, T. Baumert, S. S. Ivanov, and N. V. Vitanov, New J. Phys. **11**, 105051 (2009).
[62] U. Saalmann, S. K. Giri, and J. M. Rost, Phys. Rev. Lett. **121**, 153203 (2018).
[63] M. Li, P. Zhang, S. Luo, Y. Zhou, Q. Zhang, P. Lan, and P. Lu, Phys. Rev. A **92**, 063404 (2015).
[64] N. A. Hart, J. Strohaber, A. A. Kolomenskii, G. G. Paulus, D. Bauer, and H. A. Schuessler, Phys. Rev. A **93**, 063426 (2016).
[65] A. Bunjac, D. B. Popovic, and N. S. Simonovic, Phys. Chem. Chem. Phys. **19**, 19829 (2017).
[66] A. Bunjac, D. B. Popovic, and N. S. Simonovic, Phys. Lett. A **394**, 127197 (2021).
[67] B. Kaufman, T. Rozgonyi, P. Marquetand, and T. Weinacht, Phys. Rev. A **103**, 023108 (2021).
[68] P. V. Demekhin and L. S. Cederbaum, Phys. Rev. A **86**, 063412 (2012).
[69] S. B. Zhang and N. Rohringer, Phys. Rev. A **89**, 013407 (2014).
[70] C. Yu and L. B. Madsen, Phys. Rev. A **98**, 033404 (2018).
[71] S. Chatterjee and T. Nakajima, Phys. Rev. A **96**, 063406 (2017).
[72] A. Tóth and A. Csehi, J. Phys. B **54**, 035005 (2021).
[73] A. Assion, T. Baumert, J. Helbing, V. Seyfried, and G. Gerber, Chem. Phys. Lett. **259**, 488 (1996).
[74] A. Bunjac, D. B. Popovic, and N. S. Simonovic, Eur. Phys. J. D **71**, 208 (2017).
[75] Y. Boran, N. Hart, N. Kaya, J. Zhou, A. A. Kolomenskii, and H. A. Schuessler, J. Phys. B **54**, 145401 (2021).
[76] D. Tannor, *Introduction to Quantum Mechanics: A Time-Dependent Perspective* (University Science Books, Herndon, 2005).
[77] B. Kaufman, T. Rozgonyi, P. Marquetand, and T. C. Weinacht, Phys. Rev. A **102**, 063117 (2020).
[78] D. A. Tumakov, D. A. Telnov, G. Plunien, and V. M. Shabaev, Phys. Rev. A **100**, 023407 (2019).
[79] T. Morishita and C. D. Lin, Phys. Rev. A **87**, 063405 (2013).
[80] S.-D. Jheng and T. F. Jiang, J. Phys. B **50**, 195001 (2017).
[81] M. Schuricke, K. Bartschat, A. N. Grum-Grzhimailo, G. Zhu, J. Steinmann, R. Moshammer, J. Ullrich, and A. Dorn, Phys. Rev. A **88**, 023427 (2013).
[82] M. Schuricke, G. Zhu, J. Steinmann, K. Simeonidis, I. Ivanov, A. Kheifets, A. N. Grum-Grzhimailo, K. Bartschat, A. Dorn, and J. Ullrich, Phys. Rev. A **83**, 023413 (2011).
[83] J. Mitroy, M. S. Safronova, and C. W. Clark, J. Phys. B **43**, 202001 (2010).

[84] H.-W. Li, S. Kar, and P. Jiang, Int. J. Quantum Chem. **113**, 1493 (2013).
[85] B. K. Sahoo and B. Arora, Phys. Rev. A **87**, 023402 (2013).
[86] S. Balay *et al.*, PETSc Users Manual, ANL-95/11, revision 3.14, 2021, available at https://petsc.org/release/docs/.
[87] L. Dalcin, P. Kler, R. Paz, and A. Cosimo, Adv. Water Resources **34**, 1124 (2011).
[88] V. Hernandez, J. E. Roman, and V. Vidal, ACM Trans. Math. Softw. **31**, 351 (2005).
[89] H. Hellmann, J. Chem. Phys. **3**, 61 (1935).
[90] M. S. Pindzola *et al.*, J. Phys. B **40**, R39 (2007).
[91] T. N. Rescigno and C. W. McCurdy, Phys. Rev. A **62**, 032706 (2000).
[92] T. J. Park and C. J. Light, J. Chem. Phys. **85**, 5870 (1986).
[93] W.-C. Jiang and X.-Q. Tian, Opt. Express **25**, 26832 (2017).